



3D Reconstruction of Active Regions with STEREO

Markus J. Aschwanden and Jean-Pierre Wülser

Solar and Astrophysics Laboratory, Lockheed Martin, Advanced Technology Center, 3251 Hanover St., Bldg. 252, Org. ADBS, Palo Alto, CA 94304, USA

Abstract

We review data analysis and physical modeling related to the 3D reconstruction of active regions in the solar corona, using stereoscopic image pairs from the STEREO/EUVI instrument. This includes the 3D geometry of coronal loops (with measurements of the loop inclination plane, coplanarity, circularity, and hydrostaticity), the 3D electron density and temperature distribution (which enables diagnostics of hydrostatic, hydrodynamic, and heating processes), the 3D magnetic field (independent of any theoretical model based on photospheric extrapolations), as well as the 3D reconstruction of CME phenomena, such as EUV dimming, CME acceleration, CME bubble expansion, and associated Lorentz forces that excite MHD kink-mode oscillations in the surroundings of a CME launch site. The mass of CMEs, usually measured from white-light coronagraphs, can be determined independently from the EUV dimming in the CME source region. The full 3D density and temperature structure of an active region can be reconstructed in unprecedented detail with instant stereoscopic tomography.

Keywords: solar corona, active regions, stereoscopy, tomography

1. Introduction

The importance of three-dimensional (3D) reconstruction in astrophysics can hardly be overstated. Without stellar parallax measurements we would not know the distance to the stars, we would not be able to tell apart supernovas from our milky way or from other galaxies, nor would we know about the expanding universe. Similarly, the STEREO mission has opened up our 3D vision on the Sun and in the heliosphere, where we can use the stereoscopic parallax to triangulate coronal loops (Feng et al. 2007a; Aschwanden et al. 2008a), active regions, polar plumes (Feng et al. 2009), polar jets (Patsourakos et al. 2008), filaments (Gissot et al. 2008; Liewer et al. 2009), prominences, and coronal mass ejections (e.g., Wood et al. 2009). 3D reconstruction

Email address: aschwanden@lmsal.com (Markus J. Aschwanden and Jean-Pierre Wülser)

URL: <http://www.lmsal.com/~aschwand/> (Markus J. Aschwanden and Jean-Pierre Wülser)

of structures in the solar corona has been attempted already in the pre-STEREO era, using solar-rotation stereoscopy and tomography (e.g., Berton and Sakurai 1985; Koutchmy and Molodensky 1992; Aschwanden and Bastian 1994; Frazin 2000), but this approach requires quasi-stationary structures over a time interval of a quarter solar rotation (≈ 7 days), which are hard to find in the highly dynamic corona. A particular method of “dynamic stereoscopy” was developed that allows for dynamic plasma flows along coronal loops, but relies on the quasi-stationarity of the guiding magnetic field (Aschwanden et al. 1999a). Only after the launch of the STEREO mission (August 2006) we obtained simultaneous stereoscopic image pairs that allow us to apply triangulation methods to measure directly the 3D geometry of coronal structures, using the *Extreme Ultra-Violet Imager (EUVI)* (Wülser et al. 2004). The two STEREO spacecraft are continuously separating, spanning already a separation angle of over 90° after the first four years of the mission, while classic stereoscopy was most favorable at the beginning of the mission. In this review we focus on the 3D reconstruction of active regions, which are interesting plasma physics laboratories in their own right, as well as hotbeds for coronal mass ejections (CMEs), the major science focus of the STEREO mission. Some recent reviews on 3D reconstruction with STEREO data describe theoretical modeling approaches (Aschwanden et al. 2008d), the current status of solar stereoscopy (Wiegmann et al. 2009), or solar flare and CME observations with STEREO/EUVI (Aschwanden et al. 2009c). The content of this review is organized according to different physical parameter regimes that are explored in stereoscopic 3D reconstructions of active regions, such as the 3D geometry (Section 2), the 3D electron density (Section 3), the 3D electron temperature (Section 4), the 3D magnetic field (Section 5), as well as the 3D evolution of EUV dimming (Section 6) and the 3D motion of oscillating loops (Section 7) that both accompany the launch of CMEs.

2. 3D Geometry of Active Regions

The coronal plasma is very inhomogeneous, in particular in active regions, where strong magnetic fields confine the plasma within curved coronal flux tubes. Based on the assumption of a low value of the coronal plasma- β parameter, which states that the magnetic pressure is much higher than the thermal pressure, we can conceptualize an active region in terms of numerous isolated flux tubes, which essentially are one-dimensional (1D) structures with relatively small cross-sections, so they have a high length-to-width aspect ratio of $l/w \approx 10, \dots, 10^3$. Consequently, the plasma confined in these coronal flux tubes, simply called “loops”, represent mini-atmospheres that have their own hydrodynamic structure each, and can be modeled as simple isolated 1D flux tubes. This particular nature of the magnetic field allows us to characterize coronal loops as curvi-linear 1D structures, which can conveniently be triangulated with STEREO. However, there are a number of problems that make the stereoscopic triangulation not so simple that it can be automated with a software algorithm. First of all, there exists no completely isolated loop, each one is surrounded by thousands of other loops or diffuse plasma that add confusion to the discrimination of a selected loop from the background. Therefore, only loops that have sufficient contrast in electron density and/or temperature from the surrounding background can be triangulated. Second, the identification of corresponding loops in a stereoscopic image pair A and B is often ambiguous, especially for large separation angles when the images A and B look very dissimilar. Thus, small separation angles in the order of $\alpha_{sep} \approx 5^\circ - 15^\circ$ are preferable. This requirement makes the first few months of the mission, i.e., April-June 2007, most suitable. Stereoscopy with larger separation angles is in principle possible if an approximate 3D magnetic field can be modeled, but has not yet been attempted yet. A third difficulty is

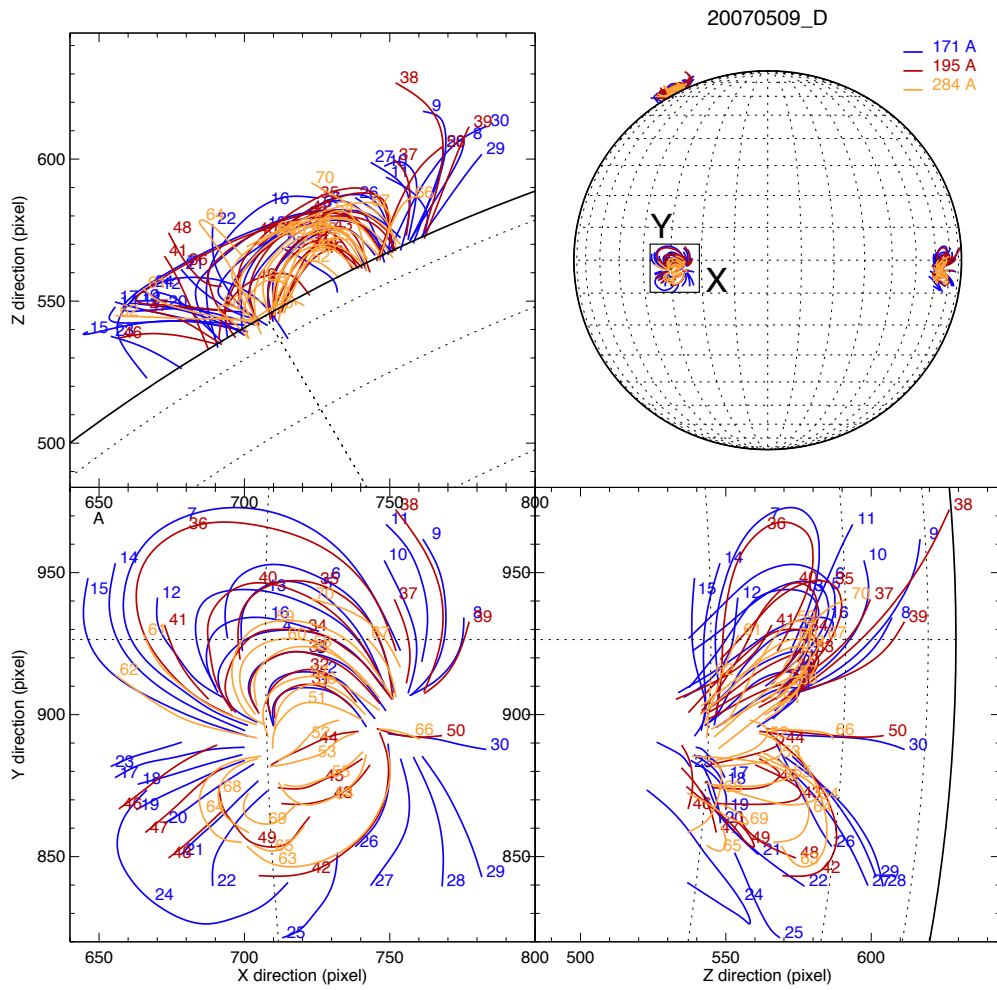


Figure 1: Orthogonal projections of the stereoscopically triangulated 70 coronal loops in AR 10955 observed on 9 May 2007 in three filters (171 Å= blue; 195 Å= red; 284 Å= yellow). The observed projection in the x-y image plane seen from spacecraft A is shown in the x-y image plane seen from spacecraft A is shown in the bottom left panel, the projection into the x-z plane is shown in the top left panel, and the projection into the y-z plane is shown in the bottom right panel. The three orthogonal projections correspond to rotations by 90° to the north or west (to positions indicated on the solar sphere in the top right panel) [Aschwanden et al. 2009a].

Table 1: Geometric and physical parameters of coronal loops reconstructed in 3D with stereoscopic triangulation using STEREO/EUVI (Aschwanden et al. 2008a,b; 2009a).

Parameter	Parameter range	Mean and standard deviation
Loop length L	24 – 243 Mm	62 ± 44 Mm
Loop width w	$\lesssim 2$ Mm	$\lesssim 1.0 \pm 1.0$ Mm
Loop aspect ratio L/w	$\gtrsim 10 - 100$	$\gtrsim 50 \pm 50$
Loop height h_{max}	11 – 71 Mm	40 ± 18 Mm
Inclination angle ϑ	$35^\circ - 73^\circ$	$55^\circ \pm 13^\circ$
Curvature radius r_{curv}	17 – 59 Mm	31 ± 11 Mm
Circularity C	3% – 30%	$13\% \pm 8\%$
Coplanarity P	3% – 13%	$8\% \pm 4\%$
Density scale height λ	30 – 120 Mm	75 ± 45 Mm
Electron density n_e	$10^{8.7} - 10^{10.3} \text{ cm}^{-3}$	$10^{9.5 \pm 0.8} \text{ cm}^{-3}$
Electron temperature T_e	0.7 – 2.7 MK	1.7 ± 1.0 MK

the confusion of loop-unrelated structures in active regions, in particular bright “moss” regions (Berger et al. 1999; DePontieu et al. 2009) that cover the central base of an active region. The moss in EUV is nothing else than the cooler transition regions ($T \approx 1 - 2$ MK) at the footpoint of hotter loops ($T \approx 2 - 8$ MK) and interferes with stereoscopic triangulation of small-scale loops in the center of active regions. A fourth difficulty is the hydrostatic scale height, which makes loops visible in EUV only within the lowest density scale height, which is approximately up to a height of $h \lesssim 50 - 100$ Mm for $T = 1 - 2$ MK loops. The resulting lack of contrast at the loop apex makes it often impossible to trace the connectivity between magnetically conjugated footpoints of the same loop, except if the loop is highly inclined. All these restrictions should be kept in mind when a stereoscopic 3D reconstruction of an active region is attempted, because it explains the biases for large inclined loops, the lack of short small-scale loops, and the missing apices of vertically oriented loops.

In Figure 1 we show an example of a stereoscopic reconstruction of the 3D geometry of some 70 loops in active region NOAA 10955, observed on 9 May 2007 with STEREO/EUVI in the wavelengths of 171, 195, and 284 Å, when the STEREO spacecraft had a separation of $\alpha_{sep} \approx 7.3^\circ$. The vertical projection (Fig. 1, top left) clearly illustrates the altitude cutoff at $h \lesssim 0.1R_\odot$ due to the hydrostatic scale height condition. The lateral projection along the dipole axis of the active region (Fig. 1, bottom right) visualizes the high inclination angles of complete loops, while there is no complete vertical large loop present, which is also a consequence of the “hydrostatic visibility condition”.

The 3D reconstruction of such a set of coronal loops that represent the skeleton of an active region involves a number of data processing steps, such as: (1) image coalignment, (2) image stacking (to improve photon statistics and signal-to-noise ratio), (3) highpass filtering (to enhance loop structures, see also Stenborg et al. 2008), (4) visual/manual or automated loop detection (Aschwanden et al. 2008c; Aschwanden 2010) or image segmentation (Inhester and Wiegelmann 2008; Feng et al. 2007a), (5) stereoscopic 3D triangulation in epipolar (coplanar with both spacecraft) geometry (Inhester 2006; Aschwanden et al. 2008a), and (6) coordinate

transformations for projections along a selected line-of-sight (e.g., in orthogonal directions as shown in Fig. 1). Geometrical parameters that can be determined with stereoscopic triangulation are: (1) The 3D coordinates $[x(s), y(s), z(s)]$ of individual loops parameterized as a function of the loop length coordinate s , (2) the true (unprojected) loop lengths L , (3) the loop widths w (also expressed as geometric aspect ratio L/w), (4) the loop apex height h_{max} , (5) the inclination angle θ of the loop plane to the vertical, (6) the loop mean curvature radius r_{curv} , (7) the degree of circularity or mean deviation from circular shape ($C = \Delta r/r_{curv}$), and (8) the degree of coplanarity or average deviation from the mean loop plane ($P = \Delta x/r_{curv}$). We list statistics of such measured parameters in Table 1. First stereoscopic coronal loop reconstructions from STEREO/SECCHI images were carried for active region NOAA 10960 observed on 8 June 2007 (Feng et al. 2007a) and for active region NOAA 10955 observed on 9 May 2007 (Aschwanden et al. 2008a).

A different technique of a 3D reconstruction method that does not make use of the concept of 1D curvi-linear loop structures has been developed by means of a local correlation tracking algorithm (Rodriguez et al. 2009). This local correlation tracking method essentially correlates identical features (of bright pixels) in a stereoscopic pair of images and triangulates the altitude for each feature. This way a range of altitudes of loop segments in an active region can automatically be determined. One example observed on 2 May 2007 (Fig. 7 in Rodriguez et al. 2009) shows a systematically higher altitude range (of $h \approx 35 - 80$ Mm) for loop segments seen in 195 \AA ($T \approx 1.5$ MK) than seen in 171 \AA ($h \approx 20 - 50$ Mm; $T \approx 1.0$ MK), which confirms the hydrostatic stratification effect (Aschwanden and Nitta 2000).

3. 3D Density Reconstruction of Active Regions

There are a number of new aspects in electron density and temperature diagnostics that can efficiently be addressed with stereoscopic data, regarding: (1) the inclination angle of loop planes, (2) diagnostics of hydrostatic versus non-hydrostatic equilibrium states, (3) super-hydrostatic dynamic flows, (4) diagnostics of coronal heating mechanisms, and (5) dense loops as tracers of the true 3D coronal magnetic field. For optically thin free-free emission in soft X-rays and in EUV wavelengths, the observed intensity scales with the square of the electron density, i.e., $I \propto n_e^2$, which implies that all bright loops have a relatively high electron density compared with the surrounding plasma. This fact, as trivial as it sounds, provides us a most powerful diagnostics of the highly inhomogeneous heating mechanisms in active regions. Coronal loops cannot attain high densities by local compression (except for short-lived shock wave structures), and thus a high density is a sure indicator of chromospheric upflows, such as occurring during the “*chromospheric evaporation process*” known in flares. Many dense and bright active region loops indeed originate as postflare loops and expand subsequently until they overarch an active region. Electron densities and related diagnostics of coronal heating processes have been performed before the STEREO mission, but a crucial issue was always the delicate choice of background subtraction, which matters so much what electron densities and (single or multiple) temperatures we infer. With stereoscopic measurements, the ambiguity of background subtraction is completely resolved, because the two different line-of-sights from the two STEREO spacecraft that intercept with a chosen loop of interest sample two independent and different backgrounds. If the background modeling is correctly done, we should end up with the same emission measure, density and temperature from two different directions, even when the background compositions along both line-of-sights are completely different (Fig. 2, right). Comparing the obtained parameters of loop densities, temperatures, and widths independently determined from both STEREO/A and

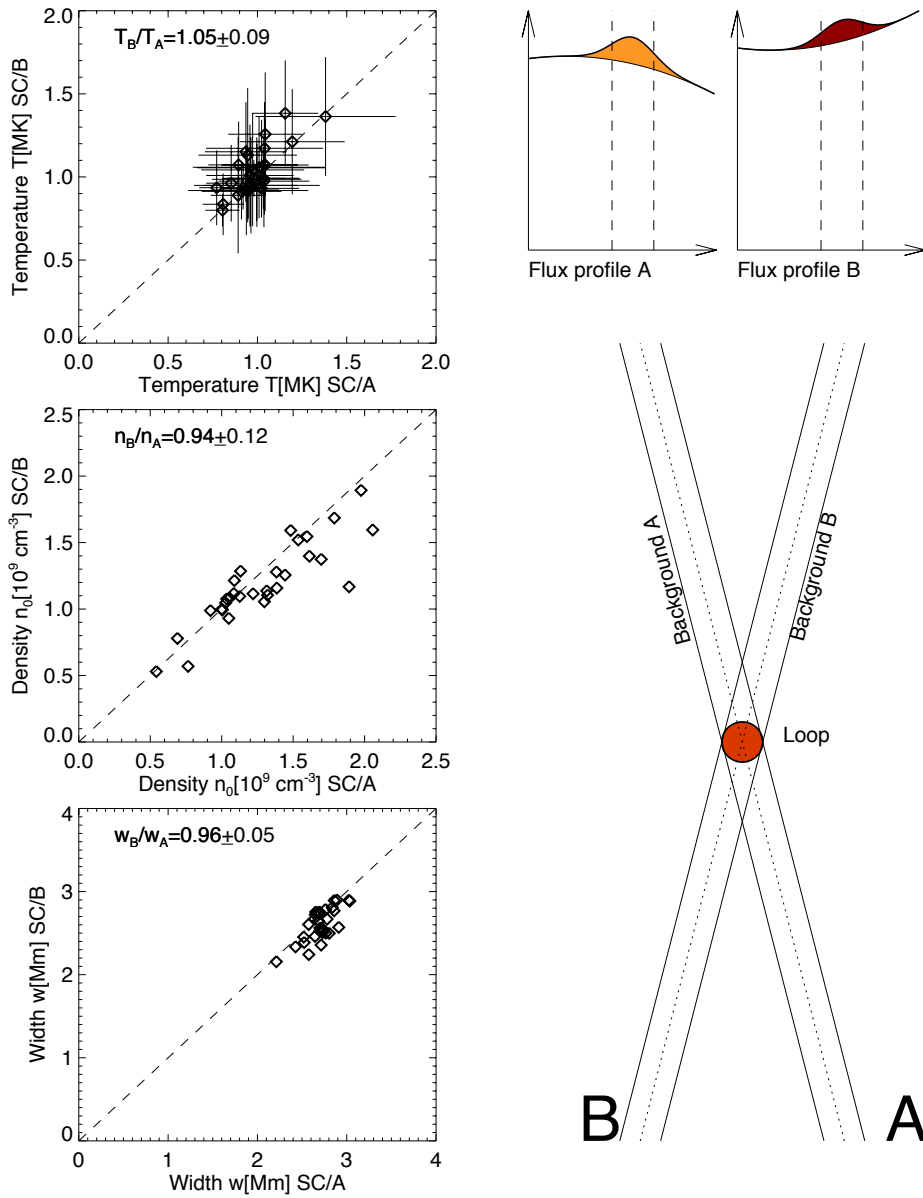


Figure 2: Self-consistency of mean loop temperatures T_A, T_B (top left), base electron densities n_A, n_B (middle left), and mean loop widths w_A, w_B (bottom left) measured with spacecraft STEREO/A vs. STEREO/B. These loop parameters are inferred from the background-subtracted loop-associated flux (top right), based on independent background subtractions for the different line-of-sights of both spacecraft A and B (bottom right) (Aschwanden et al. 2008b).

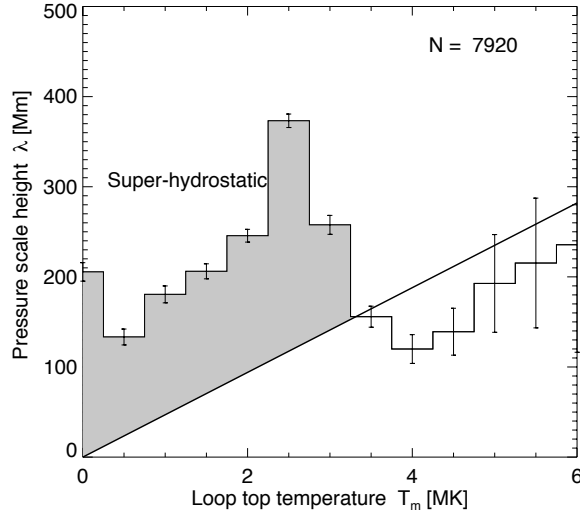


Figure 3: Average pressure scale height λ (Mm) as a function of the loop apex temperature, reconstructed for a sample of ≈ 8000 loops in AR 10955, observed with STEREO on 9 May 2007. Note that the hot ($T \approx 3 - 6$ MK) loops are near hydrostatic equilibrium, while the cooler loops ($T \approx 0.5 - 2.0$ MK) visible in EUV are super-hydrostatic (Aschwanden et al. 2009a).

B spacecraft, we could validate the accuracy of a loop background subtraction method for the first time, which was found to be in the order of $|n_e^A - n_e^B|/n_e \lesssim 10\%$ (Fig. 2, left).

Once we have established an accurate background subtraction method for the density and temperature diagnostics of coronal loops, we can diagnose various density-related physical parameters. A first obvious parameter is the determination of the (vertical) density scale height λ_T ,

$$n_e(h) = n_{e0} \exp\left(-\frac{h}{\lambda(T)}\right), \quad (1)$$

which depends linearly on the temperature T ,

$$\lambda(T) = \frac{2k_B T_e}{\mu m_H g_\odot} \approx 4.6 \times 10^9 \left(\frac{T_e}{1 \text{ MK}}\right) [\text{cm}], \quad (2)$$

where k_B is the Boltzmann constant, μ the mean molecular mass, m_H the mass of the hydrogen atom, and g_\odot is the solar gravitation, and the vertical height $h(z)$ is a function of the inclination angle ϑ to the vertical,

$$h(z) = z \cos(\vartheta), \quad (3)$$

with z being the perpendicular distance to the loop baseline in the loop plane. Thus, stereoscopic 3D triangulation provides an accurate measurement of the loop inclination angle ϑ , which allows us then to calculate the vertical scale height $\lambda(T)$ and inclined scale height $\lambda = \lambda(T)/\cos(\vartheta)$ along the loop coordinate s . If the observed scale height is larger than the theoretically expected temperature scale height $\lambda(T)$, we call the loop *super-hydrostatic*, which is an indicator of dynamic processes in the loop, such as accelerated flows (Aschwanden 2004, p.153), non-steady heating (e.g., Warren et al. 2002; Mendoza-Briceno et al. 2004), or ponderomotive wave

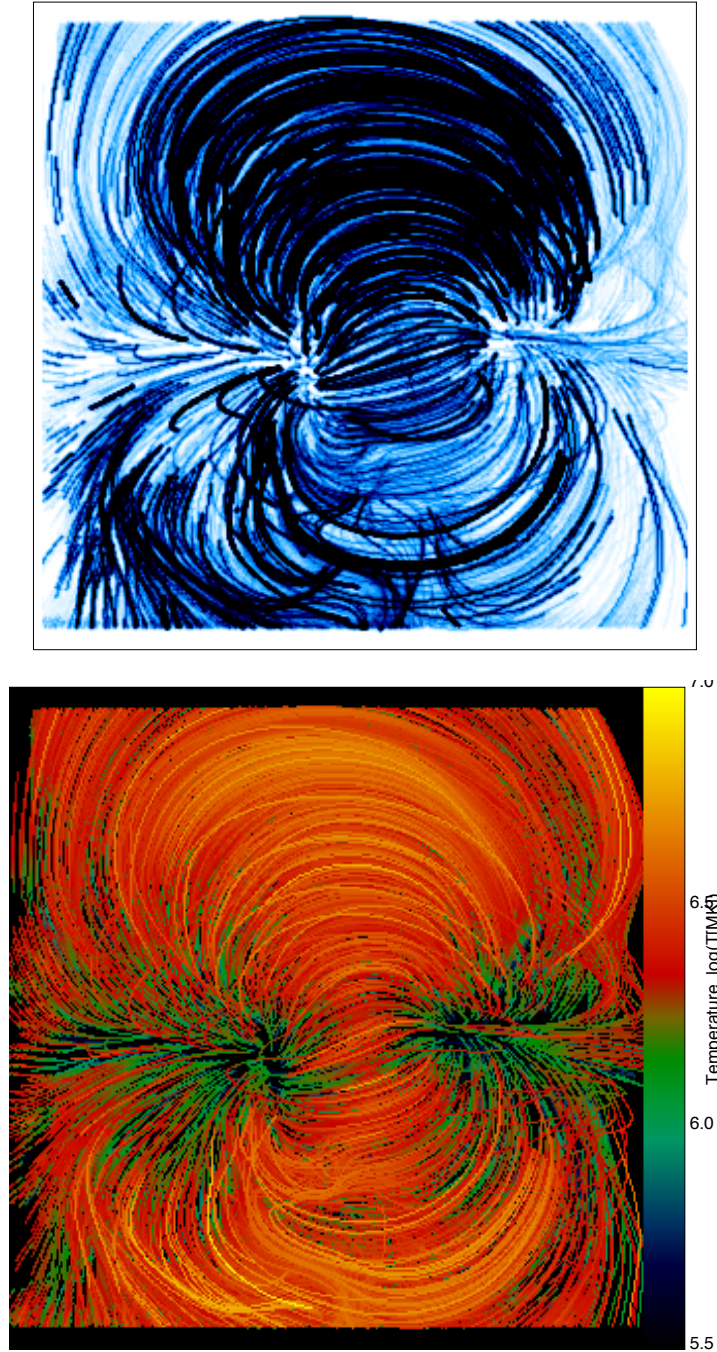


Figure 4: Density map (top) and temperature map (bottom) of active region NOAA AR 10955 observed on 9 May 2007 with STEREO/EUVI and reconstructed with the ISTAR method (Instant Stereoscopic Tomography of Active Regions). The model contains some 8000 loop components, of which a skeleton of 70 loops have been stereoscopically triangulated (Aschwanden et al. 2009a).

pressure (e.g., Litwin and Rosner 1998). Modeling of the density $n_e(s)$ and temperature profile $T_e(s)$ along the loop can also reveal whether a loop is uniformly heated (Rosner et al. 1978) or non-uniformly heated at the footpoints (Serio et al. 1981). Pre-STEREO measurements indicated that most active region loops were non-uniformly heated, display an overpressure of up to two orders of magnitude compared with the equilibrium state between heating and cooling, and evolve through a non-equilibrium state of radiative cooling when they are observed in EUV (Aschwanden and Nightingale 2005), which was fully confirmed with stereoscopic loop modeling (Aschwanden et al. 2008b). In particular, full-scale modeling of an entire active region in 3D (Aschwanden et al. 2009a) revealed that most loops at soft X-ray temperatures are nearly in hydrostatic equilibrium (which is expected during the maximum of the heating phase), but show super-hydrostatic scale heights in the EUV temperature range of $T \approx 1 - 3$ MK (as expected for the radiative cooling phase), as shown in Fig. 3.

3D Reconstruction of the solar corona can be carried out loop by loop, or for a selected coronal volume as a whole. The first method essentially corresponds to a forward-fitting of 1-D loop models, while the second approach represents a tomographic method. Since two stereoscopic spacecraft do not provide sufficient aspect angle coverage to perform classical tomography, a combined method has been developed which is called *Instant Stereoscopic Tomography of Active Regions (ISTAR)* (Aschwanden et al. 2009a). In this method, first a set of single loops is stereoscopically triangulated to provide a “3D skeleton” of the active region, then the 3D magnetic field is interpolated to provide a volume-filling set of loop coordinates, and finally each field line is filled with a parameterized hydrodynamic loop model of the electron density $n_e(s)$ and temperature $T_e(s)$ by successive forward-fitting to the 6 EUV brightness images in each of the 3 temperature filters from both spacecraft. This method provides the full 3D density distribution $n_e(x, y, z)$ and temperature distribution $T_e(x, y, z)$ of an active region. The result of such a reconstructed density map and temperature map is shown in Fig. 4.

Classical solar rotation-based tomography has previously been applied to the corona (e.g., Frazin 2000; Butala et al. 2005), which requires long-lived and quasi-steady structures, such as streamers, coronal holes, or active regions. Naturally, the spatial and temporal resolution of solar-rotation based tomography is several orders of magnitude lower than that of the ISTAR method. Tomography using STEREO COR-1 data has been recently performed to reconstruct the 3D electron density at distances from 1.5 to 4 solar radii, which can be used to double-check the locations of stereoscopically triangulated or magnetically extrapolated streamers (Kramar et al. 2009) or prominence cavities (Vasquez et al. 2009).

4. 3D Temperature Diagnostics of Active Regions

A useful characterization of the temperature distribution in a coronal structure is the *differential emission measure (DEM)* distribution $dEM(T)/dT$, which quantifies how much mass ($m = n_e m_p dV$) is contributing to the total emission in a temperature interval $[T, T + dT]$,

$$\frac{dEM(T)}{dT} = \int_V n_e^2(T) dV, \quad (4)$$

defined as the squared electron density $n_e(T)$ of plasma with a temperature in the interval $[T, T + dT]$, integrated over the total observed volume V . Normally, such a DEM distribution can only be constrained in the temperature-sensitive range of the instrument, which is $T \approx 0.7 - 2.7$ MK for the combined three STEREO/EUVI channels in 171, 195, and 284 Å. However, the stereoscopic tomography method ISTAR includes complete loops in the model, with a parameterized

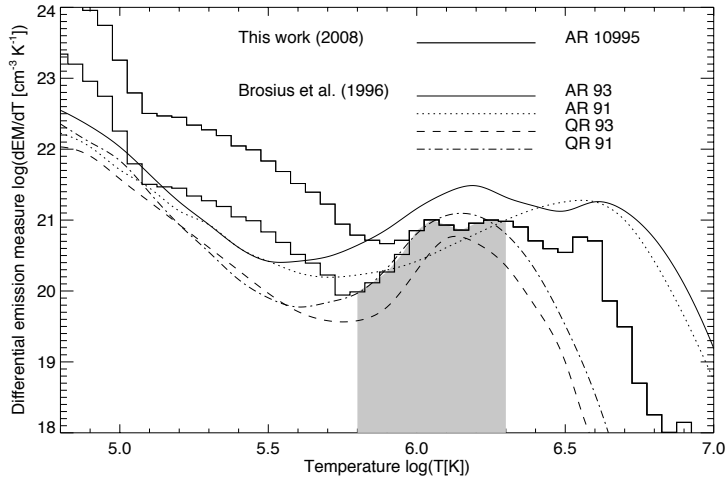


Figure 5: Differential emission measure distribution $dEM(T)/dT$ computed with the tomographic ISTAR model, compared with two active regions and two quiet Sun regions from Brosius et al. (1996). Note that the primary temperature sensitivity range of EUVI is $\log(T) \approx 5.8 - 6.3$ (grey range), but the DEM could be constrained in the range of $\log(T) \approx 4 - 7$, based on the parameterized temperature profiles used in the stereoscopic tomography code. The area of the active region is $A = 1.7 \times 10^{20} \text{ cm}^2$ and a canopy correction was applied in the temperature range of $\log(T) = 5.7 - 6.0$, with a quadratic area expansion from 10% to 100% of the coronal fluxtube area (histogram with black linestyle; the uncorrected DEM is also shown as histogram with grey color) (Aschwanden et al. 2009a).

temperature function along the loop that ranges from the cool transition region ($T \approx 10^4 \text{ K}$) up to the coronal apex temperature of the loop, which is in the range of $T \approx 1 - 8 \text{ MK}$ in typical active regions. So, the emission measure of each model loop is fitted in the geometric loop segment that falls into the observed temperature range of $T \approx 0.7 - 2.7 \text{ MK}$, while the emission measure in the lower loop segment down to the footpoint as well as in the upper loop segment up to the apex is extrapolated by the parameterized loop temperature and density model. This way, the complete DEM from $T \gtrsim 10^4 \text{ K}$ to $T \lesssim 10^7 \text{ K}$ of an active region can be reconstructed with the ISTAR method. The result of the reconstructed DEM of a stereoscopically observed active region is shown in Fig. 5. The DEM distribution is sensitive to the assumed cross-sectional loop geometry. In Fig. 5 we show one inferred DEM that assumes a constant loop cross-section (grey histogram), as well as a model of a loop canopy with an expansion from 10% to 100% in the transition region (black histogram), which follows closer to DEMs that were inferred from other instruments with a broader temperature range (Brosius et al. 1996). Thus, an observed DEM distribution can be used to model the geometry of the canopy in the transition region. A 3D tomography method to derive the DEM distribution of the entire corona with STEREO data was also developed by Frazin et al. (2009b), which allows to examine the DEM of specific structures in the corona, such as a prominence cavity for instance (Vasquez et al. 2009).

While DEMs serve to model an active region in a statistical way, the hydrodynamic density $n_e(s, t)$ and temperature structure $T_e(s, t)$ of individual loops can be efficiently modeled with stereoscopic data, because they allow us to isolate loops from the background in a more unambiguous way thanks to two independent line-of-sights. Stereoscopy also allows us to determine the loop geometry, the loop length, and inclination angle of the loop plane, which are all necessary ingredients for hydrodynamic modeling. For instance, scaling laws of hydrostatic loops, as

Table 2: Geometric and physical parameters of coronal loops reconstructed in 3D with stereoscopic triangulation using STEREO/EUVI (Aschwanden et al. 2008a,b; 2009a).

Active region	Observing time [UT]	Number of traced loops	Misalignment magnetogram extrapolation	Misalignment multi-dipole model fit
10953	2007 Apr 30, 23:00	200	$26^\circ \pm 10^\circ$	$16^\circ \pm 8^\circ$
10955	2007 May 9, 20:30	70	$19^\circ \pm 6^\circ$	$15^\circ \pm 6^\circ$
10953	2007 May 19, 12:40	100	$36^\circ \pm 13^\circ$	$24^\circ \pm 14^\circ$
10978	2007 Dec 11, 16:30	87	$32^\circ \pm 10^\circ$	$14^\circ \pm 6^\circ$

well as the determination of radiative and conductive cooling times depend all on the electron density, temperature, and loop length. Some hydrodynamic modeling of active region loops and flare loops using STEREO and Hinode data is described in Aschwanden et al. (2009c) and Aschwanden (2009c). STEREO/EUVI, which is sensitive in the temperature range of $T \approx 0.7 - 2.7$ MK, reveals plasma compressions of highly-stressed filaments or sigmoids during the impulsive phase of flares (Culhane et al. 2008; Tripathi et al. 2009; Aschwanden et al. 2009c), postflare loops in the late cooling phase of the flare, as well as tenuous high-lying coronal sources during occulted flares (Krucker et al. 2008; Aschwanden et al. 2009c). However, 3D hydrodynamic modeling of individual active region and flare loops is still in its infancy, probably due to the complexity of isolating individual loops self-consistently in different temperature filters and instruments (with STEREO, TRACE, and Hinode). The active region analyzed with the most comprehensive temperature coverage is probably NOAA 10961, which was analyzed using SOHO, TRACE, STEREO, and Hinode data (Noglik et al. 2009).

5. 3D Magnetic Field Modeling of Active Regions

The STEREO mission offers new ways to test how accurately conventional methods calculate the coronal magnetic field by using extrapolation methods from photospheric magnetograms. A measurement of the average misalignment angle between theoretical magnetic fields extrapolated from photospheric MDI magnetograms using potential field or nonlinear force-free field (NLFFF) models with stereoscopically triangulated loops using STEREO/EUVI has shown a substantial misalignment angle in the order of $20^\circ - 40^\circ$ (DeRosa et al. 2009; Sandman et al. 2009), depending on the complexity of the active region. Measurements of the average misalignment angle from four different active regions are listed in Table 2. It is thought that photospheric magnetograms do not represent a force-free vector magnetic boundary, because the magneto-convection below the photosphere is dynamic and contains significant Lorentz and buoyancy forces, which makes the approach of calculating a coronal field with a nonlinear force-free (NLFFF) code fundamentally problematic (DeRosa et al. 2009). Therefore, it is highly desirable to explore new methods that take advantage of the 3D capability of stereoscopic data.

The 3D geometry of the coronal magnetic field can be reconstructed for active regions by stereoscopic triangulation of a set of coronal loops, where each loop segment is assumed to represent the true direction of a coronal magnetic field vector. In addition, using the Maxwell equation of a divergence-free field,

$$\nabla \mathbf{B} = 0,$$

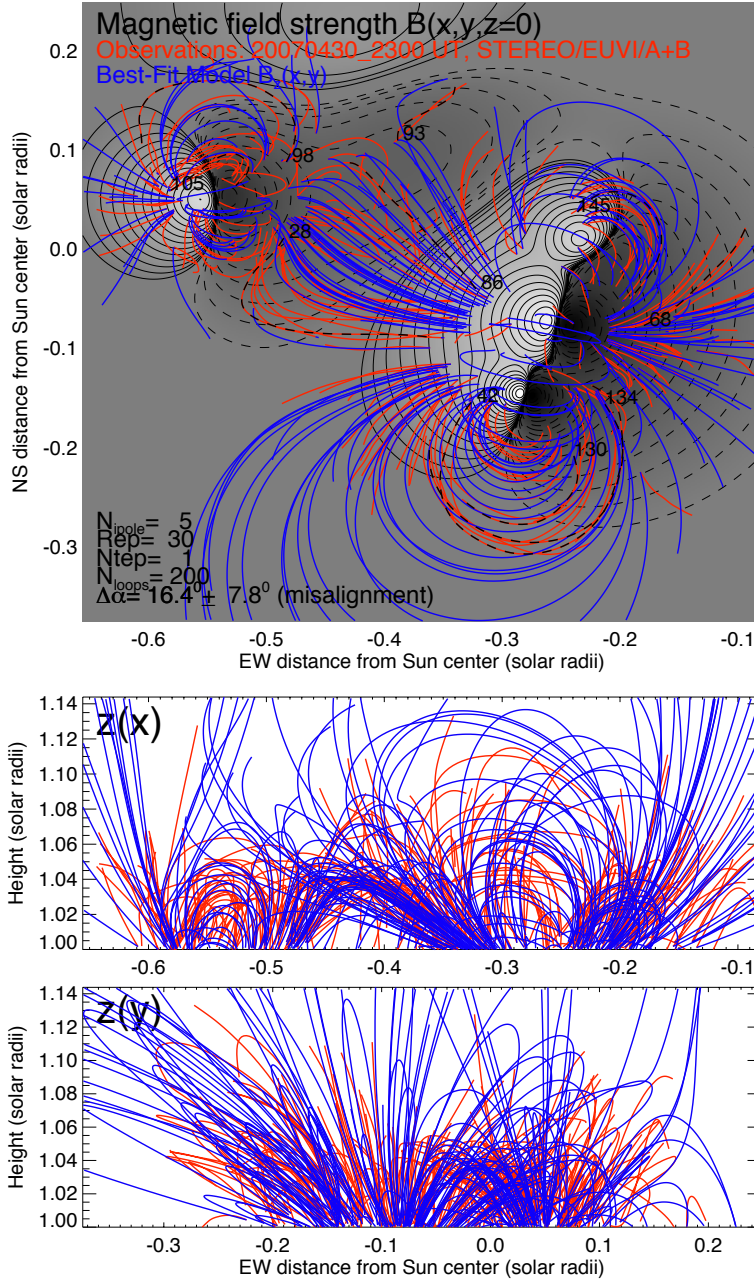


Figure 6: 3D magnetic field modeling of an active region based on STEREO data. A set of 200 loops is stereoscopically triangulated from STEREO/EUVI A and B (red curves). A parametric 3D magnetic model containing multiple ($N_{dipole} = 5$) dipole fields is fitted to the 3D coordinates of the STEREO loops, resulting in a best fit with an average misalignment angle of $\Delta\alpha = 16.4^\circ \pm 7.8^\circ$. The inferred magnetic field at the base of the corona is rendered in greyscale with contours (Aschwanden and Sandman 2010).

the dimensionless 3D magnetic field vectors \mathbf{b} ,

$$\mathbf{b}(\mathbf{x}) = \frac{\mathbf{B}(\mathbf{x})}{B_0} = \frac{1}{B_0} [B_x(x, y, z), B_y(x, y, z), B_z(x, y, z)],$$

can be reconstructed, except for the dimensional constant B_0 and its sign of the magnetic polarity. While the direct inversion of the magnetic field from stereoscopic field vectors is a numerically difficult task, a simpler approach is a forward-fitting method of a divergence-free field model to stereoscopic field vectors \mathbf{b} . We demonstrate this method by using a divergence-free field model consisting of multiple (N_D) magnetic dipoles, (e.g., Jackson 1975, p.182),

$$\mathbf{B}(\mathbf{x}) = \sum_{D=1}^{N_D} \mathbf{B}^{dip}(\mathbf{x}) = \sum_{D=1}^{N_D} \frac{3\mathbf{n}(\mathbf{n} \cdot \mathbf{m}^D) - \mathbf{m}^D}{|\mathbf{x}|^3},$$

where \mathbf{n} is a unit vector in the direction of \mathbf{x} , and \mathbf{m}^D is the magnetic moment vector of the dipole D . This multi-dipole model is a potential field and can be fitted to stereoscopic field vectors $\mathbf{b}(x, y, z)$. A best-fit solution is obtained by minimizing the misalignment angle between the theoretical field model and the observed field of coronal EUV loops inferred from STEREO. As an example we show a best-fit solution of a multi-dipole field (containing 5 dipoles) to a set of 200 stereoscopically triangulated loops observed in AR 10953 on 30 Apr 2007 in Fig. 6. The mean misalignment angle obtained with the multi-dipole model is $\alpha_{mis} = 16^\circ \pm 8^\circ$, which represents a significant improvement over conventional potential field models extrapolated from an MDI magnetogram, which produced a mean misalignment of $\alpha_{mis} = 26^\circ \pm 10^\circ$ for the same active region (Table 2).

We fitted this multiple-dipole potential field model with 6 free parameters for each dipole also to 3 other stereoscopically triangulated active regions (NOAA 10955 on 9 May 2007; NOAA 10953 on 19 May 2007; and NOAA 10978 on 11 Dec 2007) and achieved in all cases a smaller misalignment between the model and the data (Table 2), by factors of $\approx 0.4 - 0.8$ (Aschwanden and Sandman 2010). Although this model can handle up to 10 dipole components (with a total of 60 free parameters), we found that a relatively small number of ≈ 5 dipoles per active region is sufficient to obtain an improved misalignment angle of $\alpha_{mis} \lesssim 10^\circ - 20^\circ$, which is typically a factor of 0.5 better than classical magnetic field extrapolation methods. The improved results imply that the misalignment mostly originates from the fact that photospheric magnetograms are inadequate to represent the coronal field, because they are measured in non-force-free regions, while the coronal field seems to be very close to a force-free or potential field configuration.

First comparisons of stereoscopically triangulated loops with 3D magnetic field models were carried out by Feng et al. (2007a), who used a quasi-linear force-free magnetic field model (with a variable α for each loop) to solve the correspondence problem of a stereoscopic loop pair using a proximity parameter (Wiegelmann and Inhester 2006; Feng et al. 2007b). A method for solving the correspondence problem is particularly useful for large stereoscopic separation angles, where the two stereoscopic views bear no similarity at all.

STEREO observations have also been used qualitatively to clarify the magnetic topology in dynamic coronal processes (Fig. 7), such as during the flare energy build-up phase to identify a flare trigger by magnetic reconnection at a 3D null point of a separatrix surface (Su et al. 2009), multiple filament eruptions in the complex and highly nonpotential active region NOAA 10956 during 19 May 2007 (Li et al. 2008; Liewer et al. 2009), the coincidence of sigmoidal structures and their flux cancellation sites at multiple temperatures (Tripathi et al. 2009), the dipolar evolution and flux cancellation sites in coronal hole regions (Yang et al. 2009a), an emerging dipole

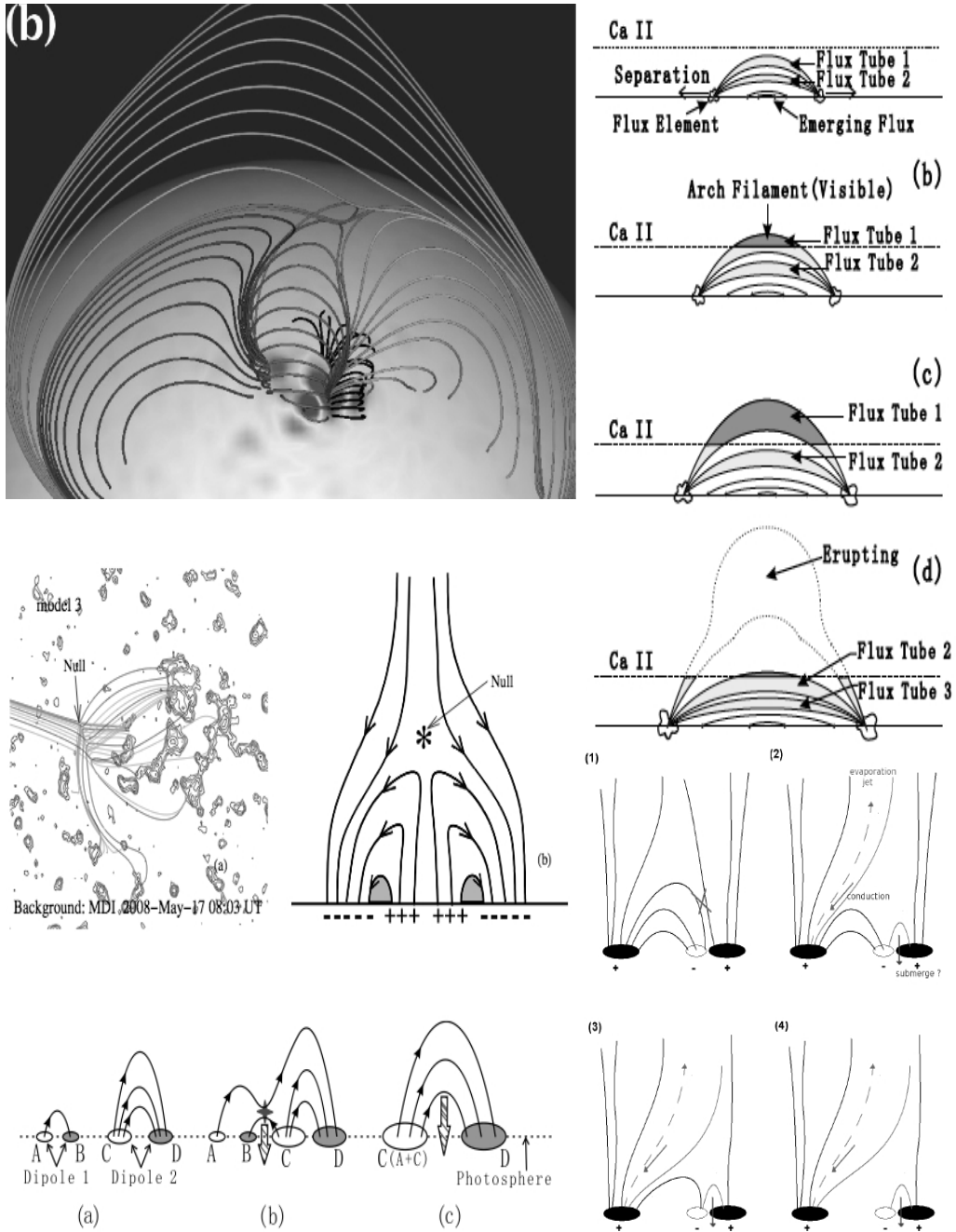


Figure 7: 3D magnetic field topology modeled with STEREO data for a filament eruption in a highly nonpotential active region (Li et al. 2008; top left); a flare triggered at a 3D null point of a separatrix surface (Su et al. 2009; middle left); a flux cancellation site in a coronal hole (Yang et al. 2009a; bottom left); an emerging dipole located at a coronal hole boundary; top right); and a magnetic flux cancellation site with a recurring solar jet (Chifor et al. 2008).

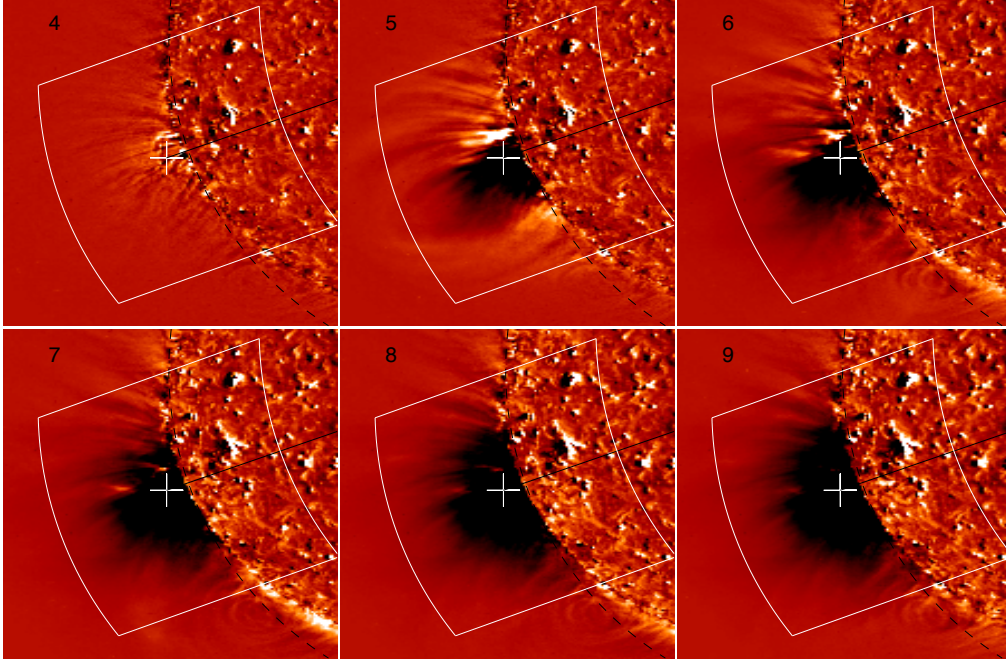


Figure 8: A sequence of 6 pre-CME subtracted difference images obtained with EUVI/A, 195 Å for a CME event observed on 31 Dec 2007, 0 – 4 UT, recorded with a cadence of 10 min. The sequence shows the progressing EUVI dimming, clearly discernible after the second frame (00:50 UT). The EUV dimming corresponds to a mass loss of $m_{CME} \approx 6 \times 10^{15}$ g (Aschwanden et al. 2009b).

located at a coronal hole boundary (Yang et al. 2009b), or magnetic flux cancellation associated with a recurring solar jet (Chifor et al. 2008).

6. 3D Reconstruction of EUV Dimming and CME mass

The STEREO mission was primarily designed to study *coronal mass ejections (CME)*. A CME usually originates in a particular active region that became magnetically unstable, causes a major magnetic re-arrangement of the active region into a lower energy state, and evacuates after launch a substantial mass fraction of the active region out into the heliosphere. CMEs typically carry a mass in the range of $m_{CME} \approx 10^{14} - 10^{16}$ g (e.g., Jackson and Hildner 1978; Howard et al. 1985; Vourlidas et al. 2000, 2002; Harrison et al. 2003; Subramanian and Vourlidas 2007), which corresponds to an average mass loss rate of $m_{CME}/(\Delta t \cdot 4\pi R_{\odot}^2) \approx 2 \times 10^{-14} - 2 \times 10^{-12}$ ($\text{g cm}^{-2} \text{s}^{-1}$), amounting to $\lesssim 1\%$ of the solar wind loss rate in coronal holes, and to $\lesssim 10\%$ in active regions, based on an average occurrence of $\Delta t \approx 1$ CME day^{-1} . A typical active region with a size of $L \approx 10^{10}$ cm, a base density of $n_e \approx 10^9 \text{ cm}^{-3}$, and a density scale height of $\lambda_T \approx 5 \times 10^9$ cm (at $T \approx 1.0$ MK) has a total mass of $m_{AR} \approx m_p n_e V \approx m_p n_e L^2 \lambda_T \approx 10^{15}$ g, which is commensurable with the mass of an average CME. The launch of a CME therefore can blow out the major part of an active region, clearing out a dark evacuation corridor in the corona that is manifested as EUV dimming, essentially creating a “*transient coronal hole*” (e.g., Rust &

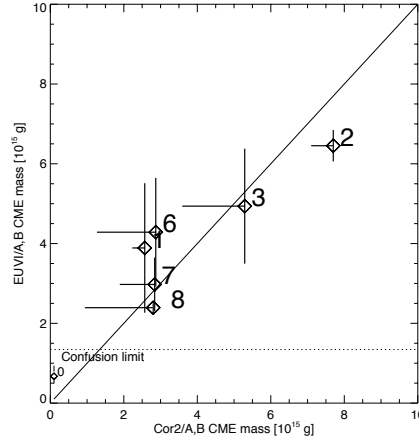


Figure 9: Comparison of CME masses measured with EUVI/A+B (y-axis) and COR2/A+B (x-axis). The diamonds mark the CME mass averaged from both EUVI/A+B spacecraft versus the 2-spacecraft constrained CME mass inferred from COR2 (corrected for the CME propagation angle to the line-of-sight). The error bars in either horizontal or vertical direction indicate the range between the measurements from spacecraft STEREO/A and B. The confusion limit of the EUV method is estimated to be $\lesssim 1.5 \times 10^{15}$ g (Aschwanden et al. 2009b).

Hildner 1976; Rust 1983), most dramatically seen in soft X-rays (e.g., Hudson & Webb 1997; Sterling & Hudson 1997).

The masses of coronal mass ejections (CMEs) have traditionally been determined from white-light coronagraphs (based on Thomson scattering of electrons), as well as from extreme ultraviolet (EUV) dimming observed with one spacecraft. Colaninno and Vourlidas (2009) measured for the first time CME masses with white-light coronagraphs from two independent spacecraft and obtained more accurate CME masses. An improved method has been recently developed (Aschwanden et al. 2009b) to measure CME masses based on EUV dimming observed with the dual STEREO/EUVI spacecraft in multiple temperature filters that includes three-dimensional volume and density modeling in the dimming region and background corona. Six CME events with previous mass determinations from STEREO/COR2 were detected with EUVI using an automated multi-wavelength detection code. An example is shown in Fig. 8 for the partially occulted CME of 31 Dec 2007. CME masses in the range of $m_{CME} = (2 - 7) \times 10^{15}$ g were determined. The agreement between the two EUVI/A and B spacecraft was $m_A/m_B = 1.3 \pm 0.6$ (Fig. 9) and the consistency with white-light measurements by COR2 is $m_{EUVI}/m_{COR2} = 1.1 \pm 0.3$. The consistency between EUVI and COR2 implies no significant mass backflows (or inflows) at $r < 4R_{\odot}$ and adequate temperature coverage for the bulk of the CME mass in the range of $T \approx 0.7 - 2.7$ MK. The temporal evolution of the EUV dimming allows us also to model the evolution of the CME density $n_e(t)$, the expanding volume $V(t)$, the height-time profile $h(t)$, and the propagation speed $v(t)$ in terms of an adiabatically expanding self-similar geometry, as shown in Aschwanden (2009b) for the CME event of 25 Mar 2008. The results of forward-fitting a 4D model (including a 3D space plus 1D temporal dimension) of an expanding CME bubble with an accelerating centroid height and bubble radius to the 25 Mar 2008 event is shown in Fig. 10, where the two STEREO spacecraft have a separation angle of $\alpha_{sep} = 47.17^\circ$, showing the CME in front and behind the limb from the two viewpoints. The

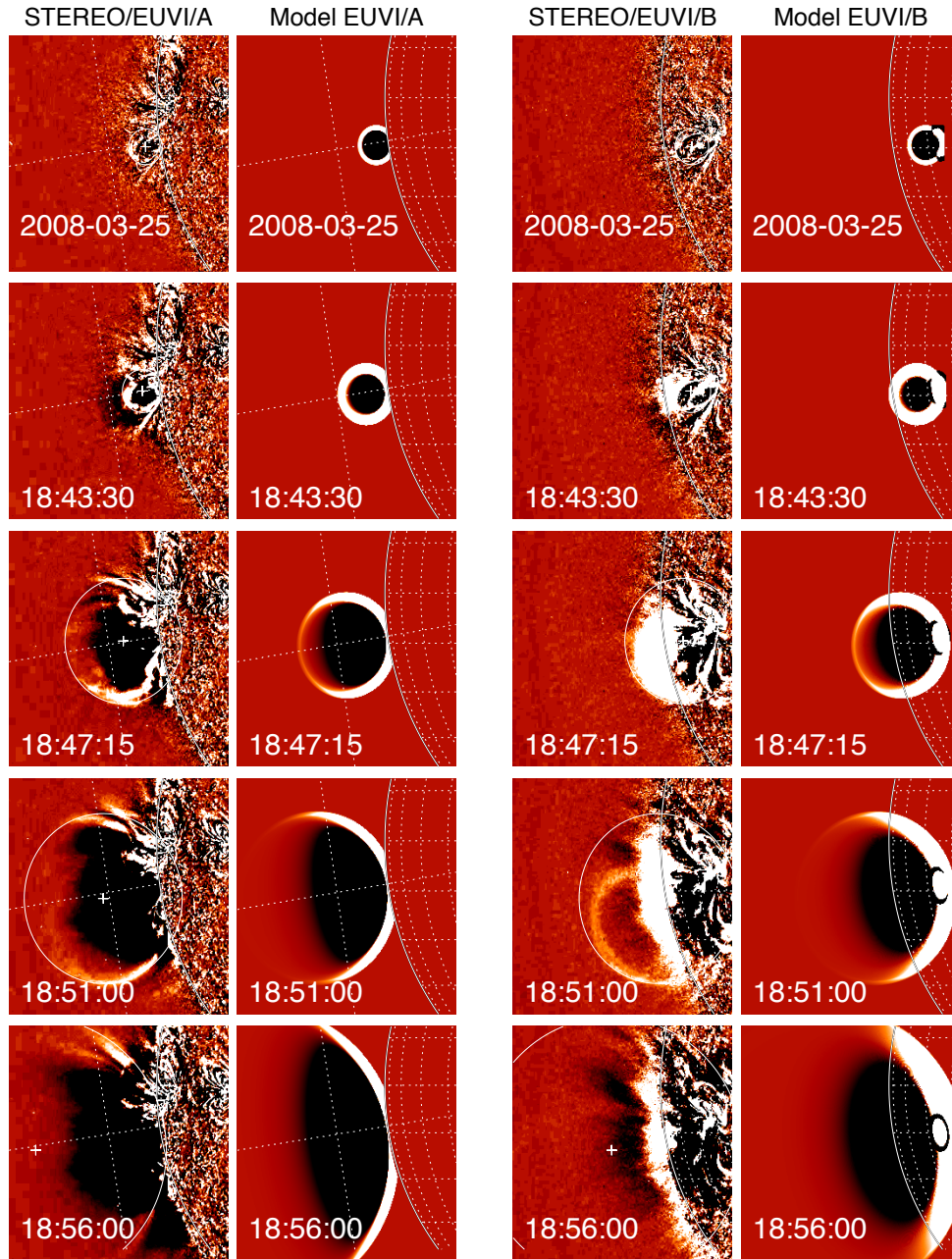


Figure 10: CME event of 25 Mar 2008: Comparison of observed and simulated EUVI base-difference images at 5 times for the observations of STEREO/A 171 Å (left two columns) and STEREO/B 171 Å (right two columns). The pre-CME image at 18:36 UT was subtracted in these base-difference images (Aschwanden 2009b).

acceleration of the CME in the beginning phase was found to be substantially higher ($a \approx 0.5 \text{ m s}^{-2}$) than measured further out in the heliosphere at $r > 4R_{\odot}$ with STEREO/COR-1. Thus the dynamic modeling in the lower corona constrain the magnetic forces that accelerate the CME during the launch phase.

Interestingly, not every CME leaves a footprint in the EUV-bright corona. For instance, in the CME event of 2 June 2008, no trace in EUV was left behind (Robbrecht et al. 2009), which is difficult to explain, indicating a launch site in the upper corona where the density is too low to be detected in EUV, or undergoing a very slow acceleration that is difficult to track in EUV. Another EUV tracer of CMEs are global waves, which sometimes even show up in soft X-rays, such as during the 23 May 2007 CME event that was simultaneously detected with Hinode/XRT and STEREO (Attrill et al. 2009). Coronal dimming, which is usually associated with a CME launch, is expected to be detected with automated algorithms in future, such as with SDO/AIA data (Attrill and Wills-Davey 2009). A similar code has been tested for automated detection of coronal holes with SOHO, STEREO and Hinode data (Krista and Gallagher 2009).

7. 3D Motion of Loop Oscillations and Waves

The launch of a CME, which evacuates often a substantial fraction of the coronal mass of an active region, causes a major disturbance in the local pressure equilibrium. Once a magnetic instability sets in that drives a filament to erupt and a CME to launch, a part of the magnetic field configuration opens up temporarily or permanently (e.g., magnetic break-out model of Antiochos et al. 1999), which is accompanied by an impulsive disturbance and adjustment of the surrounding magnetic field. It is this pressure pulse that pulls and pushes a number of surrounding coronal loops, which adjust to a new magnetic equilibrium configuration. Some mass-loaded over-dense loops (relative to the ambient coronal plasma in the active region) overshoot the new equilibrium position during this adjustment and consequently start to oscillate in the fast kink MHD mode, usually subject to strong damping, so that the kink-mode oscillations dies out after a few oscillation periods. Such MHD kink-mode loop oscillations were discovered during the 14 July 1998 flare (Aschwanden et al. 1999b), and virtually all subsequent detections of kink-mode oscillations confirmed that the trigger is always an erupting filament, flare, (Schrijver et al. 2002), or CME event (Nakariakov et al. 2009).

STEREO allows us now to reconstruct the 3D geometry and 3D motion of such oscillating loops. An example is shown in Fig. 11 for the 27 June 2007, 18 UT, flare, which was observed with both STEREO spacecraft and was analyzed by Verwichte et al. (2009) and Aschwanden (2009a). Quantitative analysis of the 3D motion of oscillating loops can provide two major diagnostics: (i) a coronal measurement of the magnetic field, and (ii) a directional 3D reconstruction of the Lorentz force that drives the CME launch and excites also the loop oscillations. The average magnetic field in the oscillating loop can be determined from the kink-mode period P_{kink} , the loop length L , and the mass densities ρ_e, ρ_0 (external and internal of the loop)

$$B = \frac{L}{P_{kink}} \sqrt{8\pi\rho_0\left(1 + \frac{\rho_e}{\rho_0}\right)}.$$

STEREO observations are extremely useful for this purpose because the full 3-D (unprojected) loop length L can be triangulated, as well as the loop density $n_0 = \rho_0/\mu m_H$ can be determined much more accurately thanks to two independent background measurements (see Fig. 2). Verwichte et al. (2009) determined a magnetic field strength of $B = 11 \pm 2 \text{ G}$ and an Alfvénic phase

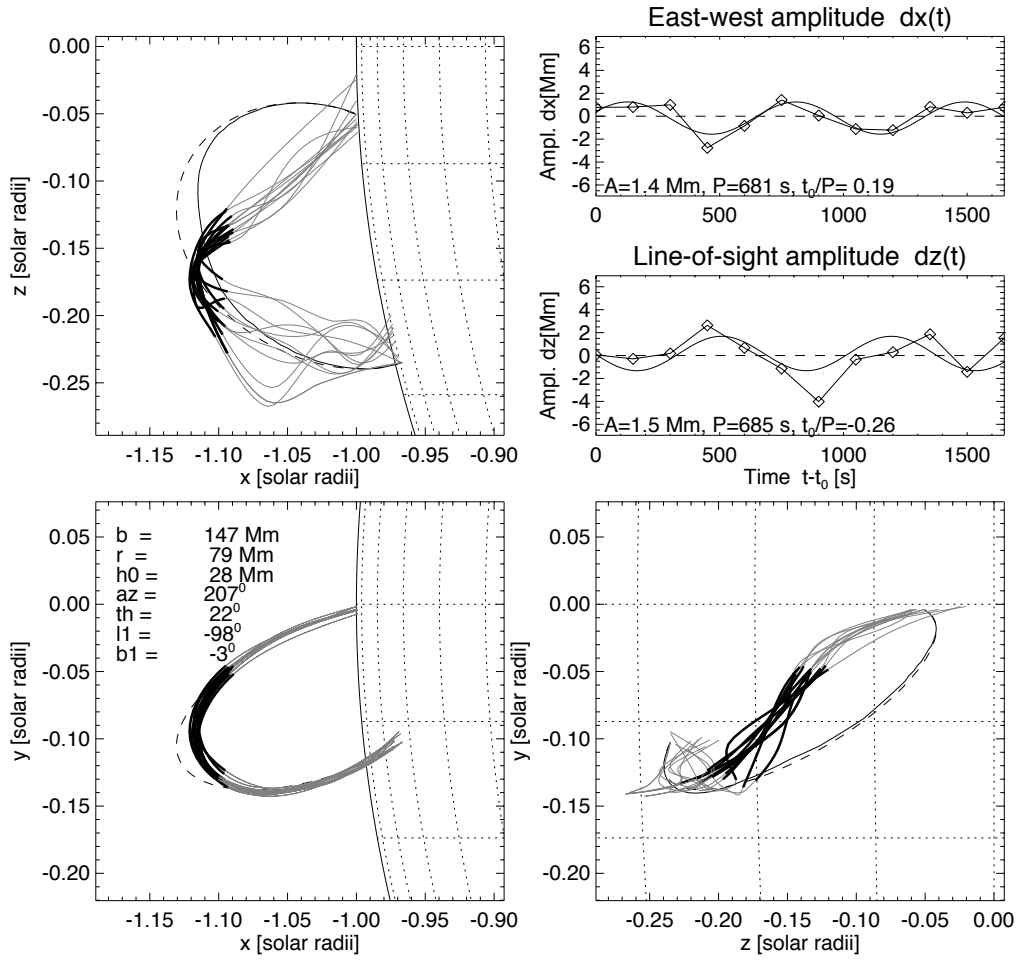


Figure 11: 3D reconstruction of loop oscillations for a sequence of 16 EUVI/A+B 171 Å images in the time interval of 2007-Jun-27, 17:58-18:26 UT, using the stereoscopic triangulation method. The loop tracings in EUVI/A are rendered in the $x - y$ plane (left bottom panel), while the orthogonal reconstruction are shown in the $x - z$ plane (top left panel) and in the $z - y$ plane (bottom right panel). The loop tracings are rendered with grey curves and the semi-circular fit with a dashed curve. The oscillation amplitudes averaged in the loop segments $0.3 < s/L < 0.6$ (marked with thick black curves) are shown in x -direction (east-west amplitude $dx(t)$ in top right panel) and in the z -direction (line-of-sight amplitude $dz(t)$ in middle right panel) (Aschwanden 2009a).

speed of $v_{ph} = 2L/P_{kink} = 1100 \pm 100 \text{ km s}^{-1}$. Aschwanden (2009a) triangulated the detailed 3-D shape of the oscillating loop and found a non-planar helical geometry and a torsional motion, which is manifested as a phase-shifted oscillation in vertical and horizontal direction to the loop (Fig. 11). Future studies with stereoscopic triangulation of multiple loops around the CME launch site might be able to reconstruct the Lorentz forces that drive the CME initiation. If the loop is dragged in the vertical direction by the plasma flow that surrounds the loop, the phenomenon of vortex shedding could possibly play a role in the kink-mode excitation (Nakariakov et al. 2009).

Future studies using 3-D MHD dynamical models in conjunction with stereoscopic 3D reconstructions have a great potential to improve the new field of coronal seismology (Ofman 2009). This is also true for diagnostics of slow (acoustic) MHD waves, which have periods P_{slow} that depend on the loop length L and sound speed c_S ,

$$P_{slow} = \frac{2L}{jc_S},$$

since the true (unprojected) loop length L can only be determined accurately with stereoscopic triangulation. It has been demonstrated that measurements with STEREO greatly improve the diagnostics of coronal slow-mode MHD waves (Marsh et al. 2009).

8. Conclusions

The STEREO mission is a very unique opportunity that provides us for the first time with the capability of stereoscopic 3D triangulation, a prerequisite for reliable 3D reconstruction of CMEs, flares, filaments, and other coronal phenomena. While the coronagraphs on STEREO are optimized to track CMEs further from $\gtrsim 1.6$ solar radii out into the heliosphere all the way to 1 AU, the EUVI imagers are ideal to study the CME origination in the lower corona up to about one density scale height ($\lesssim 1.1$ solar radii from Sun center). The ultimate goal is a deeper physical understanding of the origination of CMEs, which comes down to understand the magnetic instability that is responsible for a loss of equilibrium with subsequent expulsion of a CME. While it is not trivial to map out the coronal magnetic field in the zone of interest, usually located in a magnetically complex active region, significant steps have already been accomplished towards this direction, such as the development of a method to bootstrap the coronal magnetic field based on stereoscopic triangulation of a skeleton of active region loops, rather than using an unreliable theoretical magnetic field extrapolation model with a non-forcefree photospheric boundary. Moreover we learned to triangulate oscillating loops that were shaken by the launch of a CME, to triangulate eruptive filaments, coronal jets, and other by-products of dynamic coronal processes. Besides CME-related science, STEREO provides us also unique 3D data to study the hydrodynamics of active regions, which feeds into the fundamental questions of coronal heating, the physical modeling of the accompanying conductive and radiative cooling processes, and a deeper physical understanding of coronal seismology diagnosed from fast and slow (acoustic) MHD waves and oscillations. Numerous new results and discoveries are expected from combined MHD modeling and multi-spacecraft observations, which may involve besides STEREO also Hinode and the SDO mission.

Acknowledgements: This work was partially supported by the NASA contract NAS5-38099 of the TRACE mission, and by NASA STEREO under NRL contract N00173-02-C-2035. The STEREO/ SECCHI data used here are produced by an international consortium of the Naval

Research Laboratory (USA), Lockheed Martin Solar and Astrophysics Lab (USA), NASA Goddard Space Flight Center (USA), Rutherford Appleton Laboratory (UK), University of Birmingham (UK), Max-Planck-Institut für Sonnensystemforschung (Germany), Centre Spatial de Liège (Belgium), Institut d'Optique Théorique et Appliquée (France), Institut d'Astrophysique Spatiale (France). The USA institutions were funded by NASA; the UK institutions by the Science & Technology Facility Council (formerly the Particle Physics and Astronomy Research Council, PPARC); the German institutions by Deutsches Zentrum für Luft- und Raumfahrt e.V. (DLR); the Belgian institutions by Belgian Science Policy Office; the French institutions by Centre National d'Etudes Spatiales (CNES), and the Centre National de la Recherche Scientifique (CNRS). The NRL effort was also supported by the USAF Space Test Program and the Office of Naval Research.

References

- Antiochos, S.K., DeVore, C.R., and Klimchuk, J.A. 1999, A model for solar coronal mass ejections, *Astrophys. J.* **510**, 485-493.
- Aschwanden, M.J. and Bastian, T.S. 1994, VLA stereoscopy of solar active regions: I. Method and tests, *Astrophys. J.* **426**, 425-433.
- Aschwanden, M.J., Newmark, J.S., Delaboudiniere, J.P., Neupert, W.M., Klimchuk, J.A., Gary, G.A., Portier-Fornazzi, F., and Zucker, A. 1999a, Three-dimensional stereoscopic analysis of solar active region loops: I. SOHO/EIT observations at temperatures of 1.0-1.5 MK, *Astrophys. J.* **515**, 842-867.
- Aschwanden, M.J., Fletcher, L., Schrijver, C., and Alexander, D. 1999b, Coronal Loop Oscillations Observed with TRACE, *Astrophys. J.* **520**, 880-894.
- Aschwanden, M.J. and Nitta, N. 2000, The effect of hydrostatic weighting on the vertical temperature structure of the solar corona, *Astrophys. J.* **535**, L59-L62.
- Aschwanden, M.J. 2004, *Physics of the Solar Corona. An Introduction*, PRAXIS Inc., Chichester, UK, and Springer, Berlin.
- Aschwanden, M.J. and Nightingale, R.W. 2005, Elementary loop structures in the solar corona analyzed from TRACE triple-filter images, *Astrophys. J.* **633**, 499-517.
- Aschwanden, M.J., Wülser, J.P., Nitta, N., and Lemen, J. 2008a, First 3D reconstructions of coronal loops with the STEREO A and B spacecraft: I. Geometry, *Astrophys. J.* **679**, 827-842.
- Aschwanden, M.J., Nitta, N.V., Wülser, J.P., and Lemen, J.R. 2008b, First 3D reconstructions of coronal loops with the STEREO A and B spacecraft: II. Electron Density and Temperature Measurements, *Astrophys. J.* **680**, 1477-1495.
- Aschwanden, M.J., Lee, J.K., Gary, G.A., Smith, M., and Inhester, B. 2008c, Comparison of five numerical codes for automated tracing of coronal loops, *Solar Phys.* **248**, 359-377.
- Aschwanden, M.J., Burlaga, L.F., Kaiser, M.L., Ng, C.K., Reames, D.V., Reiner, M.J., Gombosi, T.I., Lugaz, N., et al. 2008d, Theoretical Modeling for the STEREO Mission, *Space Sci. Rev.* **136**, 565-604.
- Aschwanden, M.J. 2009a, The 3D geometry, motion, and hydrodynamic aspects of oscillating coronal loops, *Space Science Rev.*, online 24 April 2009, DOI 10.1007/s11214-009-9505-x.
- Aschwanden, M.J. 2009b, 4D-Modeling of CME expansion and EUV dimming observed with STEREO/EUVI, *Annales Geophysicae* **27**, 3275-3286.
- Aschwanden, M.J. 2009c, Hydrodynamic Modeling of Coronal Loops with Hinode and STEREO, *Astronomical Society of the Pacific Conference Series*, "The Second Hinode Workshop Science Meeting: Beyond Discovery - Toward Understanding", (eds. B.Lites, M.Cheung, T.Magara, J.Mariska, and K.Reeves), Vol. CS **415**, p.234-240.
- Aschwanden, M.J., Wülser, J.P., Nitta, N., Lemen, J., and Sandman, A. 2009a, First 3D reconstructions of coronal loops with the STEREO A and B spacecraft: III. Instant Stereoscopic Tomography of Active Regions, *Astrophys. J.* **695**, 12-29.
- Aschwanden, M.J., Nitta, N.V., Wülser, J.-P., Lemen, J.R., Sandman, A., Vourlidas, A., and Colaninno, R.C. 2009b, First Measurements of the Mass of Coronal Mass Ejections from the EUVI Dimming Observed with STEREO EUVI A and B Spacecraft, *Astrophys. J.* **706**, 376-392.
- Aschwanden, M.J., Wülser, J.P., Nitta, N., and Lemen, J. 2009c, Solar flare and CME observations with STEREO/EUVI, *Solar Phys.* **256**, 3-40.
- Aschwanden, M.J., 2010, sl A code for automated tracing of coronal loops approaching visual perception, *Solar Phys.* (in press).

- Aschwanden, M.J. and Sandman, A. 2010, *Bootstrapping the coronal magnetic field with STEREO*, (in preparation).
- Attrill, G.D.R., Engell, A.J., Wills-Davey, M.J., Grigis, P., and Testa, P. 2009, *Hinode/XRT and STEREO observations of a diffuse coronal "wave"-CME dimming event*, *Astrophys. J.* **704**, 1296-1308.
- Attrill, G.D.R., and Wills-Davey, M.J. 2009, *Automatic detection and extraction of coronal dimmings from SDO/AIA data*, *Solar Phys.*, DOI 10.1007/s11207-009-9444-4, (in press).
- Berger, T.E., DePontieu, B., Fletcher, L., Schrijver, C.J., Tarbell, T.D., and Title, A.M. 1999 *What is moss?*, *Solar Phys.* **190**, 409-418.
- Berton, R. and Sakurai, T. 1985, *Stereoscopic determination of the three-dimensional geometry of coronal magnetic loops*, *Solar Phys.* **96**, 93-111.
- Brosius, J.W., Davila, J.M., Thomas, R.J., and Monsignori-Fossi, B.C. 1996, *Measuring active and quiet sun coronal plasma properties with EUV spectra from SERTS*, *Astrophys. J. Suppl. Ser.* **106**, 143-164.
- Butala, M.D., Frazin, R. A., and Kamalabadi, F. 2005, *Three-dimensional estimates of the coronal electron density at times of extreme solar activity*, *J. Geophys. Res. (Space Physics)* **110**, 9.
- Chifor, C., Isobe, H., Mason, H.E., Hannah, I.G., Young, P.R., DeZanna, G., Krucker, S., Ichimoto, K., Katsukawa, Y., Yokoyama, T. 2008, *Magnetic flux cancellation associated with a recurring solar jet observed with Hinode, RHESSI, and STEREO/EUVI*, *Astron. and Astrophys.* **491**, 279-288.
- Colaninno, R.C. and Vourlidas, A. 2009, *First Determination of the True Mass of Coronal Mass Ejections: A Novel Approach to Using the Two STEREO Viewpoints*, *Astrophys. J.* **698**, 852-858.
- Culhane, J.L., Bone, L., Hara, H., Farrugia, C., Galvin, A., van Driel-Gesztelyi, L., Popecki, M., Luhmann, J.G., and Veronig, A. 2008, *Flare and erupting filament of 19th May, 2007 - Sources of a magnetic cloud observed by STEREO*, COSPAR Plenary Meeting, 37th COSPAR Scientific Assembly **37**, 609.
- DePontieu, B., Hansteen, V.H., McIntosh, S.W., and Patsourakos, S. 2009, *Estimating the Chromospheric Absorption of Transition Region Moss Emission*, *Astrophys. J.* **702**, 1016.
- DeRosa M.L., Schrijver, C.J., Barnes, G., Leka, K.D., Lites, B.W., Aschwanden, M.J., Amari, T., Canou, A., McTiernan, J.M., Regnier, S., Thalmann, J., Valori, G., Wheatland, M.S., Wiegelmann, T., Cheung, M.C.M., Conlon, P.A., Fuhrmann, M., Inhester, B., and Tadesse, T. 2009, *A critical assessment of nonlinear force-free field modeling of the solar corona for active region 10953*, *Astrophys. J.* **696**, 1780-1791.
- Feng, L., Inhester, B., Solanki, S., Wiegelmann, T., Podlipnik, B., Howard, R.A., and Wülser, J.P. 2007a, *First stereoscopic coronal loop reconstructions from STEREO/SECCHI images*, *Astrophys. J.* **671**, L205-L208.
- Feng, L., Wiegelmann, T., Inhester, B., Solanki, S., Gan, W. Q., Ruan, P. 2007b, *Magnetic Stereoscopy of Coronal Loops in NOAA 8891*, *Solar Phys.* **241**, 235-249.
- Feng, L., Inhester, B., Solanki, S.K., Wilhelm, K., Wiegelmann, T., Podlipnik, B., Howard, R.A., Plunkett, S.P., Wülser, J.P., and Gan, W.Q. 2009, *Stereoscopic Polar Plume Reconstructions from STEREO/SECCHI Images* *Astrophys. J.* **700**, 292-301.
- Frazin, R.A. 2000, *Tomography of the solar corona I. A robust, regularized, positive estimation method*, *Astrophys. J.* **530**, 1026-1035.
- Frazin, R.A., Jacob, M., Manchester, W.B., Morgan, H., Wakin, M.B. 2009a, *Toward Reconstruction of Coronal Mass Ejection Density from Only Three Points of View*, *Astrophys. J.* **695**, 636-641.
- Frazin, R.A., Vasquez, A.M., and Kamalabadi, F. 2009b, *Quantitative, Three-dimensional Analysis of the Global Corona with Multi-spacecraft Differential Emission Measure Tomography*, *Astrophys. J.* **701**, 547-560.
- Gissot, S.F., Hochedez, J.-F., Chainais, P., and Antoine, J.-P. 2008, *3D Reconstruction from SECCHI-EUVI Images Using an Optical-Flow Algorithm: Method Description and Observation of an Erupting Filament*, *Solar Phys.* **252**, 397-408.
- Harrison, R.A., Bryans, P., Simnett, G.M., and Lyons, M. 2003, *Coronal dimming and the coronal mass ejection onset*, *Astron. Astrophys.* **400**, 1071-1083.
- Howard, R.A., Shelley, N.R.Jr., Koomen, M.J., and Michels, D.J. 1985, *Coronal mass ejections: 1979-1981*, *J. Geophys. Res.* **90/A9**, 8173-8191.
- Hudson, H.S. and Webb, D.F. 1997, in *Coronal Mass Ejections*, Geophysical Monograph 99, (eds. N. Crooker, J.A. Joselyn, and J. Feynman), AGU Washington, DC, p.27.
- Inhester, B. 2006, *Stereoscopy basics for the STEREO mission*, eprint arXiv:astro-ph/0612649.
- Inhester, B., Feng, L., and Wiegelmann, T. 2008, *Segmentation of loops from coronal EUV images*, *Solar Phys.* **248**, 379-393.
- Jackson, J.D. 1975, *Classical Electrodynamics*, John Wiley and Sons, Inc. New York.
- Jackson, B.V. and Hildner, E. 1978, *Forerunners - Outer rims of solar coronal transients*, *Solar Phys.* **60**, 155-170.
- Koutchmy, S. and Molodensky, M.M. 1992, *Three-dimensional image of the solar corona from white-light observations of the 1991 eclipse*, *Nature* **360**, 717.
- Kramar, M., Jones, S., Davila, J., Inhester, B., and Mierla, M. 2009, *On the Tomographic Reconstruction of the 3D Electron Density for the Solar Corona from STEREO COR1 Data*, *Solar Phys.* (in press).

- Krista, L.D., and Gallagher, P.T. 2009, *Automated Coronal Hole Detection Using Local Intensity Thresholding Techniques*, Solar Phys. 256, 87-100.
- Krucker, S., Saint-Hilaire, P., Christe, S., White, S.M., Chavier, A.D., Bale, S.D., Lin, R.P. 2008, *Coronal Hard X-Ray Emission Associated with Radio Type III Bursts*, Astrophys. J. 681, 644-649.
- Li, Y., Lynch, B.J., Stenborg, G., Luhmann, J.G., Huttunen, K.E.J., Welsch, B.T., Liewer, P.C., and Vourlidas, A. 2008, *The Solar Magnetic Field and Coronal Dynamics of the Eruption on 2007 May 19*, Astrophys. J. 681, L37-L40.
- Liewer, P.C., DeJong, E.M., Hall, J.R., Howard, R.A., Thompson, W.T., Culhane, J.L., Bone, L., and VanDriel-Gesztelyi, L. 2009, *Stereoscopic analysis of the 19 May 2007 erupting filament*, Solar Phys. 256, 57-72.
- Litwin, C. and Rosner, R. 1998, *Coronal scale-height enhancement by magnetohydrodynamic waves*, Astrophys. J. 506, L143-L146.
- Marsh, M.S., Walsh, R.W., and Plunkett, S. 2009, *3D coronal slow modes: towards 3D seismology*, Astrophys. J. 697, 1674-1680.
- Mendoza-Briceno, C.A., Erdelyi, R., and Sigalotti, L.Di.G. 2004, *The effects of stratification on oscillating coronal loops* Astrophys. J. 605, 493-502.
- Nakariakov, V.M., Aschwanden, M.J., and Van Doorselaere, T. 2009, *The possible role of vortex shedding in the excitation of kink-mode oscillations in the solar corona*, Astron. Astrophys. 502, 661-664.
- Nogliki, J.B., Walsh, R.W., and Maclean, R.C. 2009, *Deconstructing active region AR 10961 using STEREO, Hinode, TRACE, and SOHO*, Astrophys. J. 703, 1923-1938.
- Ofman, L. 2009, *Progress, Challenges, and Perspectives of the 3D MHD Numerical Modeling of Oscillations in the Solar Corona*, Space Science Rev. (in press).
- Patsourakos, S., Pariat, E., Vourlidas, A., Antiochos, S.K., and Wülser, J.P. 2008, *STEREO/SECCHI stereoscopic observations constraining the initiation of polar coronal jets*, Astrophys. J. 680, L73-L76.
- Robbrecht, E., Patsourakos, S., and Vourlidas, A. 2009, *No Trace Left Behind: STEREO Observation of a Coronal Mass Ejection Without Low Coronal Signatures*, Astrophys. J. 701, 283-291.
- Rodriguez, L., Zhukov, A. N., Gissot, S., and Mierla, M. 2009, *Three-Dimensional Reconstruction of Active Regions*, Solar Phys. 256, 41-55.
- Rosner, R., Tucker, W.H., and Vaiana, G.S. 1978, *Dynamics of quiescent solar corona*, Astrophys. J. 220, 643-665.
- Rust, D.M. and Hildner E. 1976, *Expansion of an X-ray coronal arch into the outer corona*, Solar Phys. 48, 381-387.
- Rust, D.M. 1983, *Fast-moving fronts in solar flare loops*, in Proc. "Solar Physics and Interplanetary Travelling Phenomena", (eds. C.deJager and Chen Biao), Science Press, Beijing.
- Sandman, A., Aschwanden, M.J., DeRosa, M., Wülser, J.P., and Alexander, D. 2009, *Comparison of STEREO/EUVI Loops with Potential and Force-Free Magnetic Field Models*, Solar Phys. 259, 1-11.
- Schrijver, C.J., Aschwanden, M.J., and Title, A. 2002, *Transverse Oscillations in Coronal Loops Observed with TRACE: I. Movies, an Overview of Events, and the Identification of Required Conditions*, Solar Phys. 206, 69-98.
- Serio, S., Peres, G., Vaiana, G.S., Golub, L., and Rosner, R. 1981, *Closed coronal structures. II generalized hydrostatic model*, Astrophys. J. 243, 288-300.
- Stenborg, G., Vourlidas, A., and Howard, R.A. 2008, *A Fresh View of the Extreme-Ultraviolet Corona from the Application of a New Image-Processing Technique*, Astrophys. J. 674, 1201-1206.
- Sterling, A.C. and Hudson, H.S. 1997, *Yohkoh observations of X-ray dimming associated with a halo coronal mass ejection*, Astrophys. J. 491, L55-L58.
- Su, Y.N., VanBallegoijen, A., Schmieder, B., Berlicki, A., Guo, Y., Golub, L., and Huang, G. 2009, *Flare energy build-up in a decaying active region near a coronal hole*, Astrophys. J. 704, 341-353.
- Subramanian, P. and Vourlidas, A. 2007, *Energetics of solar coronal mass ejections*, Astron. Astrophys. 467, 685-694.
- Tripathi, D., Kliem, B., Mason, H., Young, P., and Green, L. 2009, *Temperature tomography of a coronal sigmoid supporting the gradual formation of a flux rope* Astrophys. J. 698, L27-L32.
- Vasquez, A.M., Frazin, R.A., Kamalabadi, F. 2009, *3D Temperatures and Densities of the Solar Corona via Multi-Spacecraft EUV Tomography: Analysis of Prominence Cavities*, Solar Phys. 256, 73-85.
- Verwichte, E., Aschwanden, M.J., Van Doorselaere, T., Foullon, C., and Nakariakov, V.M. 2009, *Seismology of a large coronal loop from EUVI/STEREO observations of its transverse oscillation*, Astrophys. J. 698, 397-404.
- Vourlidas, A., Subramanian, P., Dere, K.P., and Howard, R.A. 2000, *Large-angle spectrometric coronagraph measurements of the energetics of coronal mass ejections (with LASCO)*, Astrophys. J. 534, 456-467.
- Vourlidas, A., Buzasi, D., Howard, R. A., and Esfandiari, E. 2002, *Mass and energy properties of LASCO CMEs*, in "Solar Variability: From Core to outer Frontiers", Proc. 10th European Solar Physics Meeting, European Space Agency Special Publication Vol. 506, (ed. Wilson, A.), ESA, ESTEC Noordwijk, The Netherlands, p.91-94.
- Warren, H.P., Winebarger, A.R., and Hamilton, P.S. 2002, *Hydrodynamic modeling of active region loops*, Astrophys. J. 579, L41-L44.
- Wiegelmann, T. and Inhester, B. 2006, *Magnetic stereoscopy* Solar Phys. 236, 25-40.
- Wiegelmann, T., Inhester, B., and Feng, L. 2009, *Solar stereoscopy - Where are we and what developments do we require to progress?*, Annales Geophysicae 27/7, 2925-2936.

- Wood, B.E., Howard, R.A., Thernmisien, A., Plunkett, S.P., and Socker, D.G. 2009, *Reconstructing the 3D morphology of the 17 May 2008 CME*, Solar Phys. (submitted).
- Wülser, J.P., Lemen, J.R., Tarbell, T.D., Wolfson, C.J., Cannon, J.C., Carpenter, B.A., Duncan, D.W., Gradwohl, G.S., et al. 2004, *The STEREO-SECCHI Extreme Ultraviolet Imager (EUVI)*, SPIE **5171**, 111-122.
- Yang, S.H., Zhang, J., and Borrero, J.M. 2009a, *Dipolar evolution in a coronal hole region*, Astrophys. J. (in press).
- Yang, S.H., Zhang, J., Jin, C.L., Li, L.P., and Duan, H.Y. 2009b, *Response of the solar atmosphere to magnetic field evolution in a coronal hole region*, Astron. Astrophys. **501**, 745-754.